

# Label-free high-resolution 3-D imaging of gold nanoparticles inside live cells using optical diffraction tomography

Doyeon Kim<sup>a,b,d†</sup>, Nuri Oh<sup>c,d†</sup>, Kyoohyun Kim<sup>a,d</sup>, SangYun Lee<sup>a,d</sup>, Jiho Park<sup>c,d\*</sup>, YongKeun Park<sup>a,b,d\*</sup>

<sup>a</sup>Department of Physics, Korea Advanced Institute of Science and Technology (KAIST), Daejeon 34141, South Korea

<sup>b</sup>Tomocube, Inc., Daejeon 34051, South Korea

<sup>c</sup>Department of Bio and Brain Engineering, KAIST, Daejeon 34141, South Korea

<sup>d</sup>KI for Health Science and Technology (KIHST), KAIST, Daejeon 34141, South Korea

†these authors contribute equally to this work.

\*corresponding authors: Y.K.P ([yk.park@kaist.ac.kr](mailto:yk.park@kaist.ac.kr)); J.P ([jihopark@kaist.ac.kr](mailto:jihopark@kaist.ac.kr))

**Delivery of gold nanoparticles (GNPs) into live cells has high potentials, ranging from molecular-specific imaging, photodiagnosics, to photothermal therapy. However, studying the long-term dynamics of cells with GNPs using conventional fluorescence techniques suffer from phototoxicity and photobleaching. Here, we present a method for 3-D imaging of GNPs inside live cells exploiting refractive index (RI) as imaging contrast. Employing optical diffraction tomography, 3-D RI tomograms of live cells with GNPs are precisely measured for an extended period of time with sub-micrometre resolution. The locations and contents of GNPs in live cells are precisely addressed and quantified due to their distinctly high RI values, which was validated by confocal fluorescence imaging of fluorescent dye conjugated GNPs. We present segmentations of GNPs from cytosols and perform quantitative analysis of the volume distribution of aggregated GNPs as well as the temporal evolution of GNPs contents in HeLa and 4T1 cells.**

Gold nanoparticles (GNPs) have been widely applied to biological cell studies in various research fields because of their distinctive properties which differentiate them from conventional biomolecules and even from other metal nanoparticles<sup>1</sup>. GNPs exhibit surface plasmon resonance which arises from the collective oscillation of conduction electrons by incident photons in a specific wavelength, resulting in the strong absorption of light at the specific wavelength. In addition, the size and shape of GNPs can be controlled by various synthesis techniques<sup>1</sup> for spectral multiplexing. Moreover, GNPs show relatively high chemical stability compared to other metal nanoparticles. With these unique properties, the current uses of GNPs can be listed from photodiagnosis to photothermal therapy<sup>2-6</sup>.

In order to visualize GNPs inside cells and investigate the effects of GNPs, various imaging techniques have been implemented. While transmission electron microscopy (TEM) conventionally provides high spatial resolution images of GNPs, TEM requires the extremely vacuum and high-intensity electron beam, thus incompatible with live cells<sup>7,8</sup>. Fluorescence imaging techniques, such as epifluorescence microscopy and confocal microscopy, have been utilized for observing the spatial distribution of GNPs inside biological cells. By tagging fluorescent dyes to the functionalized surface of GNPs, these fluorescence techniques provide high molecular specificity in live cell imaging<sup>9,10</sup>. However, fluorescent probes may alter the original physiological conditions of biological cells and may also suffer from phototoxicity and photobleaching<sup>11,12</sup>. In addition, three-dimensional (3-D) fluorescence imaging requires the axial scanning scheme, which suffers long acquisition time for 3-D images<sup>13</sup>.

Holographic microscopy has been employed in imaging GNPs inside live cells, because gold has distinct refractive index (RI) values compared to cellular components, resulting in detectable optical phase shifts of the incident light. Warnasooriya *et al.* have used heterodyne digital holographic microscopy to localize a single GNP attached to the cellular surface receptor<sup>14</sup>. Turko *et al.* have utilized wide-field interferometric phase microscopy to detect the photothermal phase signals from GNPs inside cells<sup>15</sup>. Previous techniques have measured 2-D complex optical fields, and numerical propagation of the measured optical fields by employing the angular spectrum method can localise the 3-D positions of single GNPs<sup>16</sup>. However, these previous approaches have exhibited poor axial resolution that cannot be applied for volumetric reconstructions of complicated shaped or aggregated GNPs and cells. More importantly, 2-D complex optical fields only provide optical phase shift images, in which RI values and shapes of objects are coupled.

Recently, optical diffraction tomography (ODT) has emerged as a label-free 3-D imaging technique, which can measure the 3-D RI distribution of biological samples in high spatial resolution<sup>16,17</sup>. Since the RI is an intrinsic optical property of material, ODT does not need additional labeling agent. Because ODT takes into account of light diffraction inside samples and reconstructs the 3-D RI distribution of samples from measured complex optical fields, ODT can be applied for visualization of complicated structures of samples which cannot be explored by angular spectrum method<sup>18</sup>. Moreover, ODT provides quantitative information of biological samples from measured 3-D RI distribution, including protein concentration, cellular dry mass, and volume. Due to aforementioned advantages of ODT, it has been widely used to study various biological samples such as red blood cell<sup>19-21</sup>, phytoplankton<sup>22</sup>, and human downy hair<sup>23</sup>.

Here, we present label-free high-resolution 3-D imaging of GNPs in live cells by implementing ODT. Employing an ODT system based on a Mach-Zehnder interferometer and a digital micromirror device (DMD), the 3D RI tomograms of individual live cells with GNPs were measured. To reconstruct a 3-D RI tomogram, multiple 2-D optical field images of individual live cells were obtained with various illumination angles which are controlled by using a DMD, and then a reconstruction algorithm to inverse light scattering was applied. The measured tomograms showed that RI values of GNPs are significantly higher than other intracellular components in cells. Using this fact, GNPs were successfully segmented from cytoplasm with high spatial resolution, which was confirmed by confocal fluorescence imaging. Using the present technique, we quantitatively analysed the time evolution of GNPs volume ratios inside two different cancer cell lines (HeLa and 4T1), which clearly showed the accumulation of GNPs inside cells

## Results

**Principles of imaging GNPs with ODT.** The schematic procedure for imaging GNPs in live cells using ODT is depicted in Fig. 1(a). Prepared PEGylated GNPs were uptaken by cells before measurements (See Methods). Live cells are placed between coverslips with a spacer and measured with an ODT system. Multiple 2-D holograms are measured with various illumination angles as shown in the subsets in Fig. 1(a). From the each measured hologram, an optical field image consisting of amplitude and phase images are retrieved by applying a field retrieval algorithm<sup>24</sup>. From the multiple 2-D optical field images, the 3-D RI distribution of a sample was reconstructed using the ODT algorithm based on the Fourier diffraction theorem (See Methods)<sup>23,24</sup>.

**Experimental setup.** In order to measure 3-D RI distributions of cells, we utilized commercialized ODT setups (HT-1S and HT-1H, Tomocube, Inc., South Korea). The schematic of the setup is shown in Fig. 1(b). The system is based on a Mach-Zehnder interferometric microscope equipped with a DMD. A laser beam from a diode-pumped solid-state laser ( $\lambda = 532$  nm, 10 mW) is divided into two arms. One beam is used as a reference beam, and the other beam illuminates a sample with various incident angles ranging from  $-60^\circ$  to  $60^\circ$ . In order to control the angle of incident illumination, a digital micromirror device (DMD, DLP6500FYE, Texas Instruments, United States) was implemented. By projecting a Lee hologram pattern on a DMD, the angle of the diffracted light from the DMD was precisely controlled by applying corresponding hologram patterns<sup>25,26</sup>. The beam diffracted from the sample was collected by using a  $60\times$  objective lens, and then was interfered with the reference beam, generating spatially modulated holograms. The holograms of a sample were recorded with a high-speed image sensor (CMOS camera, FL3-U3-13Y3M-C, FLIR Systems, Inc., United States) with a frame rate of 300 Hz. The results in Fig. 1 and Fig. 4 were obtained with an objective lens with a numerical aperture (NA) of 1.2, and the rest of results were obtained with an objective lens with an NA of 0.8. The theoretical optical lateral and axial resolution of the present method are calculated as 166 nm and 1.00  $\mu\text{m}$  for NA = 0.8, and 110 nm and 356 nm for NA = 1.2.

**Synthesis and characterization of GNPs.** GNPs (average diameter = 20 nm) were synthesized and further coated with methoxy-polyethyleneglycol (mPEG)-sulfhydryl (5k) molecules following the standard protocol<sup>18</sup>. PEGylated GNPs were stable under the experimental condition, and HeLa cells can take up individual nanoparticles. HeLa cells were treated with PEGylated GNPs solution in a cell culture medium for 6 h prior to the measurements (see Methods).

Representative 3-D RI tomograms of GNPs inside a HeLa cell are shown in Figs. 1(c)–(e). Figure 1(c) shows cross-sectional slices of the 3-D RI tomogram in the  $x$ - $y$ ,  $x$ - $z$ , and  $y$ - $z$  planes of a HeLa cell treated with PEGylated GNPs, and 3-D rendered image of the same cell is shown in Fig. 1(d). The reconstructed 3-D RI distribution of endocytosed GNPs in the HeLa cell have regions with RI values, which are distinctively higher than those of cytoplasm. We consider these regions as the complex or aggregated GNPs, which are highlighted in Fig. 1(e).

Synthesized GNPs were characterized by utilizing various methods [Figs. 2(a)–(e)]. First, transmission electron micrographs of citrate- and PEGylated GNPs are presented in Figs. 2(a)–(b), which showed their spherical shapes with uniform diameters of about 20 nm. The absorption spectra of citrated and PEGylated GNPs did not change significantly [Fig. 2(a)], indicating that no aggregation generated during surface modification in aqueous conditions. The hydrodynamic diameters of PEGylated GNPs, which were measured using a dynamic light scattering instrument (Zetasizer Nano ZS90, Malvern Instruments Ltd., United Kingdom), were slightly larger than that of citrated GNPs because of organic molecules coated on the surface [Figure 2(b)].

**Comparisons between native and GNPs treated cells.** In order to determine the RI distributions of GNPs inside biological cells, we measured 3-D RI tomograms of GNPs treated ( $n = 15$ ) and native cells ( $n = 15$ ). From the measured RI tomograms of cells, average RI histograms were calculated [Fig. 2(e)]. In order to exclude surrounding media from the calculation, voxels with RI values higher than that of surrounding media ( $n > 1.337$ ) were only selected from the measured RI tomograms, which correspond to cells. As shown in Fig. 2(e), GNPs treated cells showed RI distributions in which the distributions exhibit higher RI values compared

to those of native cells. The maximum RI value of native cells was about 1.385, whereas that of GNPs treated cells was about 1.42. It is noteworthy that reported values RI of cell cytoplasm were within the range of 1.37-1.39. Cytoplasm, consisting of protein solutions in physiological concentrations<sup>27-29</sup>, does not exhibit RI values higher than 1.4, except for hemozoin crystals in malaria-infected red blood cells<sup>20</sup> or lipid droplets in hepatocyte<sup>30</sup>. These regions with RI values higher than usual cytoplasm are assumed to correspond to GNPs.

**RI values of GNPs in colloidal and aggregated forms.** To understand the high RI values measured in cells with GNPs, we measured RI values of GNPs. Due to the limited spatial resolving power of ODT, reconstructed RI tomograms were sampled with a finite voxel size of  $110 \times 110 \times 356$  nm and  $166 \times 166 \times 1,000$  nm for the high and low NA objective lenses, respectively. Furthermore, because of their spherical shapes, GNPs does not fill 100% of a specific voxel even for the case of externally highest concentration of colloidal or aggregations. Thus, the measured RI values should reflect the volume concentration of GNPs.

First, we RI values of GNPs in colloidal forms in transparent media. Various concentrations of GNPs, expressed as optical density (OD) values, are dispersed in phosphate buffered saline solution (PBS solution, pH 7.4, 50 mM, Welgene, South Korea), and the RI values of solutions are measured with Fourier transform light scattering technique<sup>31,32</sup> (See Methods). The measured RI values as a function of OD are shown in Fig. 2(f). The measured RI of the PBS solution without GNPs are  $1.343 \pm 0.006$ , which are in good agreement with the manufacturer's specification. The measured RI values for the GNP solutions increased with the concentrations of GNPs; the RI values for the GNP solutions with ODs of 0.5, 2, and 4 are  $1.346 \pm 0.006$ ,  $1.348 \pm 0.005$ , and  $1.353 \pm 0.006$ , respectively. Although the measured RI values increased as the concentrations of GNPs, even the average RI values of the densest solution (OD = 4) was 1.353. However, the 3-D RI tomograms showed that the presence of GNPs inside cells causes the regions with RIs higher than 1.385 [Fig. 2(e)]. Furthermore, it is physiologically unlikely that GNPs in live cell would have the concentration of higher than OD of 4.

Because the colloidal solutions of GNPs do not exhibit high RI values which we have been observed in GNPs treated cells, we hypothesized that the GNPs in cells would be in the aggregated form. To test this hypothesis, we added NaCl to the colloidal GNPs solution in order to trigger the aggregation of GNPs, and measured 3-D RI tomograms of the GNP solutions with NaCl. As shown in Figs. 2(g)–(h), we observed highly aggregated parts which showed high RI values ( $n > 1.38$ ). This high values of RI correspond to those appeared in the GNPs treated cells. These results suggest that portions of GNPs exist in the form of highly aggregated forms, which can be imaged and identified by measuring 3-D RI tomograms of the GNP-treated cells.

**Correlation with confocal fluorescent images.** To confirm that the regions having higher RI values inside cells represent GNPs, we compared RI tomograms of HeLa cells having PEGylated GNPs with confocal fluorescent images of the same cells. For the confocal imaging, PEGylated GNPs were further conjugated with Alexa Fluor 555 dyes. After GNPs treatment, cells were fixed by using 4% paraformaldehyde to prevent further movements of GNPs inside cells. Then, intracellular distributions of GNPs were visualized using laser scanning confocal microscope (LSCM, C2+, Nikon Instruments Inc., Japan). In order to acquire 3-D fluorescent images, samples were scanned along the axial direction at 20 different focal planes with the axial step of 0.21  $\mu$ m. Total acquisition time for scanning all 20 planes was 20 min. Figures 3(a)–(c) show the representative images of a HeLa cell having PEGylated GNPs measured by a differential interference contrast (DIC) microscope, LSCM, and ODT, respectively. Voxels with RI values higher than 1.38 show high spatial correlation with fluorescent signals of confocal images, notwithstanding some nonmatching regions. Nevertheless, such nonmatching regions do not possess significant portions and voxels with RI values higher than 1.38 take 0.5 % of total volume of native cells as calculated from RI histograms, supporting that the standard of  $n = 1.38$  can be used in the imaging of GNPs with ODT.

**Quantitative analysis.** Quantitative analysis for the size of aggregated GNPs inside cells has been carried out. First, the total number of aggregated GNPs was counted, and their volume ratio to total cellular volume was calculated for the sample represented in Figs. 4(a)–(c). Among the voxels with RI values higher than  $n > 1.38$ , a group of connected voxels was considered as one aggregated GNPs and the volume of each group was

calculated. In order to minimize the effect of noises, we excluded groups with size less than three voxels from the calculation. The total number of aggregated GNPs were 800, and the volume fraction of those GNPs to the cellular volume ( $1.57 \times 10^3 \mu\text{m}^3$ ) was 7.08%. Furthermore, the volume distribution of aggregated GNPs was organized and compared with the result for 10 different samples as shown in Fig. 4(d). Groups of aggregated GNPs with volume smaller than  $0.1 \mu\text{m}^3$  were considered as ‘weakly aggregated GNPs’, and those with bigger volume were considered as ‘highly aggregated GNPs’. The distribution of weakly aggregated GNPs showed a non-Gaussian distribution that the number of groups continuously decreased as the volume increased. The average number of highly aggregated GNPs for 10 cells was  $24.5 \pm 5.8$ .

Then, we quantitatively measured the temporal evolution of volumetric ratios of GNPs inside HeLa cells during the GNPs treatment times (0 min, 5 min, 1 h, 3 h, and 6 h). RI tomograms of 10 cells for each treatment time were acquired as shown in Fig. 5(a), from which cellular volume and the volume of GNPs were calculated by integrating voxels with RI values higher than  $n > 1.337$  and  $n > 1.38$ , respectively. The volume proportion of GNPs inside HeLa cells increases from 0.123% at 0 min to 12.2% after 6 h of GNPs treatment [Fig. 5(b)]. The results imply that GNPs are continuously transported into HeLa cells, which is in good agreement with previous reports<sup>33-35</sup>. This result is also confirmed with another mammalian cell line (4T1 cell, murine breast cancer cell) as the volume proportion of GNPs inside 4T1 cells ( $n = 10$ ) increases from 0.073% at 0 min to 30.7% after 6 h of GNPs treatment [Figs. 5(c)-(d)]. These results demonstrate the ability of ODT as a tool for the quantitative 3-D analysis of nanoparticles because the axial scanned 2-D image set of confocal microscopy does not provide the information for axial connectivity between particles as well as the size of resulted point spread function can be varied along the gain and laser intensity.

## Discussion

We present a label-free 3-D imaging method for measuring the 3-D spatial distribution of GNPs inside live cells by employing ODT. The 3-D RI distribution of GNPs inside live cells reconstructed via ODT shows significantly high RI values ( $n > 1.38$ ) compares to surrounding cytoplasm, which was also confirmed with fluorescence images of the same GNPs. This fact was applied for the segmentation of the spatial distribution of GNPs from measured RI tomograms of cells. In addition, the present method provides quantitative analysis of the volume distribution of aggregated GNPs and time evolution of the transport of GNPs inside various types of mammalian cell lines.

Possible errors can come out from the use of specific cells containing cellular materials with high RI values comparable to GNPs. For example, lipid droplets and carbohydrates inside cells have RI values overlapped with those of GNPs, which means present method cannot resolve them from GNPs inside cells. In addition, the sensitivity of present method should be increased in order to visualize GNPs in colloidal and weakly aggregated forms. It is expected that the employment of hyperspectral ODT<sup>36,37</sup> or external photothermal excitation of GNPs<sup>38</sup> can resolve this problem by obtaining the dispersion of GNPs for a different wavelength or by detecting photothermal signals from GNPs which are expressed as the changes in phase delay maps.

We expect that the present technique can be utilized for cancer targeting by the conjugation of GNPs with tumour binding antibodies<sup>39</sup>. Moreover, the image stitching method can expand the field of view which are suitable for tissue imaging<sup>17</sup> as well as this approach can be employed in the long-term tracking of GNPs in tissues by using tissue phase imaging techniques and compact live cell incubators. Furthermore, recent developments of beam scanning devices and detectors in ODT enable the fast acquisition of the 3-D RI distribution of samples with the tomogram acquisition rate of 100 Hz<sup>25,40,41</sup>. Recently, several commercial ODT instruments were released, and thus, lowering barriers to entry for the active use of ODT in research areas such as biomedical imaging and disease diagnostics. In a sense, this work shows not only the new GNPs imaging method but also one of the possible biological applications of ODT.

## Methods

**Tomogram reconstruction** From multiple 2-D optical fields various illumination angles, the 3-D RI distribution of a sample was reconstructed via an ODT algorithm<sup>29,42</sup>. In the ODT algorithm, each 2-D Fourier spectra information corresponding to a 2-D complex optical fields obtained with a specific incident angle was mapped onto a spherical surface, called Ewald sphere, in the 3-D Fourier space, according to Fourier diffraction theorem. Because an objective lens has a limited numerical aperture (NA) for collecting diffracted light from a sample, the mapped Fourier space inevitably has a certain amount of missing information, which is known as called the missing cone. To fill the missing information, we applied Gerchberg-Papoulis algorithm with a non-negativity constraint. The details in this algorithm can be found in the previous reports<sup>23,42,43</sup>. Finally, the 3-D RI distribution of the sample was reconstructed by applying inverse 3-D Fourier transform of the 3-D Fourier space. More details about the principle of ODT, the ODT algorithm, and the Gerchberg-Papoulis algorithm can be found elsewhere<sup>29,42,44,45</sup>. Reconstruction and visualization of the 3-D RI tomograms were performed using commercial software (TomoStudo, Tomocube Inc., Republic of Korea)

**Cell culture and GNPs treatment** Human cervical cancer cell line, HeLa cell, was maintained in Dulbecco's modified Eagle's medium (DMEM). Murine breast cancer cell line, 4T1 cell, was maintained in RPMI 1640 medium in 37°C humidified incubator (5% CO<sub>2</sub>, 95% air). PEGylated and fluorescent GNPs were made from colloidal GNPs with diameter 20 nm. Each GNPs was added to the cell suspension at 150 μM Au ion concentration and incubated for 6 h. at 37°C.

**Fourier transform light scattering** Fourier transform light scattering (FTLS) was used to calculate RI values for a GNPs solution<sup>31,32</sup>. First, 2-D field images of colloidal solutions of GNPs with silica beads of known RI value ( $n = 1.4607$  at  $\lambda = 532$  nm) were taken. From the measured field image, the far-field angle-resolved light scattering spectra of silica beads were calculated by applying 2-D Fourier transformation. According to the Mie scattering theory, the angle-resolved light scattering spectra is analytically determined from the RI and size of a spherical scatter, the RI of a medium ( $n = 1.4607$ ), and the wavelength of incident light ( $\lambda = 532$  nm). Fitting the measured angle-resolved light scattering spectra to the Mie scattering theory provide information about the GNP solution, because the other parameters were known. Calculations of the Fourier transform light scattering and fittings to the Mie theory were performed using a custom MatLab code.

**Preparation of PEGylated GNPs and fluorescence-conjugated GNPs** For PEGylated 20 nm GNPs, 20 mL of 1.0 mM HAuCl<sub>4</sub> was brought to a boil in a 100 mL bottle, and then 1.6 mL of 38.8 mM tri-sodium citrate was added. The solution colour changed from clear to bright red and dark red over 5 minutes. To modify surface of GNPs with methoxy polyethylene glycol (mPEG, 5K), 25 mg of mPEG was added in bare GNPs solution and was vortexed for overnight at room temperature. After synthesis and surface modification, hydrodynamic size of the GNPs was characterized using dynamic light scattering and TEM. In order to conjugate Alexa fluor 555 Succinimidyl Ester (AF555, ThermoFisher Scientific, United States) dye with GNPs, 20 mg of mPEG and 5 mg NH<sub>2</sub>-PEG was added to citrated GNPs and dialysed for 2 days. 5.0 μg μL<sup>-1</sup> of AF555 was added to the GNPs solution and vortexed for overnight at room temperature. Excess dyes were removed via centrifugation.

## ACKNOWLEDGEMENTS

This work was supported by KAIST, Tomocube, and the National Research Foundation of Korea (2015R1A3A2066550, 2014M3C1A3052567, 2014K1A3A1A09063027) .

## AUTHOR CONTRIBUTIONS

Y.K.P and J.P conceived and supervised the project. D.K and N.O performed experiments and analysed the data. K.K and S.Y.L analysed the data and discussed the results. All authors wrote the manuscript.

## COMPETING FINANCIAL INTERESTS

Prof. Park has financial interests in Tomocube Inc., a company that commercializes optical diffraction tomography and quantitative phase imaging instruments and is one of the sponsors of the work.

## References

- 1 Ghosh, S. K. & Pal, T. Interparticle coupling effect on the surface plasmon resonance of gold nanoparticles: from theory to applications. *Chemical reviews* **107**, 4797-4862 (2007).
- 2 Balasubramanian, S. K. *et al.* Characterization, purification, and stability of gold nanoparticles. *Biomaterials* **31**, 9023-9030 (2010).
- 3 Grzelczak, M., Pérez-Juste, J., Mulvaney, P. & Liz-Marzán, L. M. Shape control in gold nanoparticle synthesis. *Chemical Society Reviews* **37**, 1783-1791 (2008).
- 4 Durr, N. J. *et al.* Two-photon luminescence imaging of cancer cells using molecularly targeted gold nanorods. *Nano Lett* **7**, 941-945 (2007).
- 5 El-Sayed, I. H., Huang, X. & El-Sayed, M. A. Selective laser photo-thermal therapy of epithelial carcinoma using anti-EGFR antibody conjugated gold nanoparticles. *Cancer letters* **239**, 129-135 (2006).
- 6 Huang, X., El-Sayed, I. H., Qian, W. & El-Sayed, M. A. Cancer cell imaging and photothermal therapy in the near-infrared region by using gold nanorods. *Journal of the American Chemical Society* **128**, 2115-2120 (2006).
- 7 Huang, X., Jain, P. K., El-Sayed, I. H. & El-Sayed, M. A. Gold nanoparticles: interesting optical properties and recent applications in cancer diagnostics and therapy. (2007).
- 8 Pitsillides, C. M., Joe, E. K., Wei, X., Anderson, R. R. & Lin, C. P. Selective cell targeting with light-absorbing microparticles and nanoparticles. *Biophysical journal* **84**, 4023-4032 (2003).
- 9 Chithrani, B. D., Ghazani, A. A. & Chan, W. C. Determining the size and shape dependence of gold nanoparticle uptake into mammalian cells. *Nano Lett* **6**, 662-668 (2006).
- 10 Kourkoutis, L. F., Plitzko, J. M. & Baumeister, W. Electron microscopy of biological materials at the nanometer scale. *Annual review of materials research* **42**, 33-58 (2012).
- 11 Sousa, F. *et al.* Functionalized gold nanoparticles: a detailed in vivo multimodal microscopic brain distribution study. *Nanoscale* **2**, 2826-2834 (2010).
- 12 Zhang, Y. & Hensel, M. Evaluation of nanoparticles as endocytic tracers in cellular microbiology. *Nanoscale* **5**, 9296-9309 (2013).
- 13 Fei, Y. *et al.* Fluorescent labeling agents change binding profiles of glycan-binding proteins. *Molecular BioSystems* **7**, 3343-3352 (2011).
- 14 Hoebe, R. *et al.* Controlled light-exposure microscopy reduces photobleaching and phototoxicity in fluorescence live-cell imaging. *Nature biotechnology* **25**, 249-253 (2007).
- 15 Shang, L. *et al.* Facile preparation of water-soluble fluorescent gold nanoclusters for cellular imaging applications. *Nanoscale* **3**, 2009-2014 (2011).
- 16 Warnasooriya, N. *et al.* Imaging gold nanoparticles in living cell environments using heterodyne digital holographic microscopy. *Optics Express* **18**, 3264-3273 (2010).
- 17 Turko, N. A., Peled, A. & Shaked, N. T. Wide-field interferometric phase microscopy with molecular specificity using plasmonic nanoparticles. *Journal of biomedical optics* **18**, 111414-111414 (2013).
- 18 Lee, K. *et al.* Quantitative phase imaging techniques for the study of cell pathophysiology: from principles to applications. *Sensors* **13**, 4170-4191 (2013).
- 19 Park, H. *et al.* Characterizations of individual mouse red blood cells parasitized by *Babesia microti* using 3-D holographic microscopy. *Scientific Reports* **5** (2015).
- 20 Kim, K., Kim, K. S., Park, H., Ye, J. C. & Park, Y. Real-time visualization of 3-D dynamic microscopic objects using optical diffraction tomography. *Optics Express* **21**, 32269-32278 (2013).
- 21 Park, H. *et al.* Three-dimensional refractive index tomograms and deformability of individual human red blood cells from cord blood of newborn infants and maternal blood. *Journal of biomedical optics* **20**, 111208-111208 (2015).
- 22 Lee, S. *et al.* High-Resolution 3-D Refractive Index Tomography and 2-D Synthetic Aperture Imaging of Live Phytoplankton. *Journal of the Optical Society of Korea* **18**, 691-697 (2014).

- 23 Kim, K. *et al.* High-resolution three-dimensional imaging of red blood cells parasitized by *Plasmodium falciparum* and in situ hemozoin crystals using optical diffraction tomography. *Journal of biomedical optics* **19**, 011005-011005 (2014).
- 24 Debnath, S. K. & Park, Y. Real-time quantitative phase imaging with a spatial phase-shifting algorithm. *Optics Letters* **36**, 4677-4679 (2011).
- 25 Shin, S., Kim, K., Yoon, J. & Park, Y. Active illumination using a digital micromirror device for quantitative phase imaging. *Optics letters* **40**, 5407-5410 (2015).
- 26 Shin, S. *et al.* Optical diffraction tomography using a digital micromirror device for stable measurements of 4-D refractive index tomography of cells. *Proc. of SPIE* **9718**, 971814 (2016).
- 27 Lee, K. *et al.* Quantitative phase imaging techniques for the study of cell pathophysiology: from principles to applications. *Sensors* **13**, 4170-4191 (2013).
- 28 Popescu, G. *Quantitative Phase Imaging of Cells and Tissues*. (McGraw-Hill Professional, 2011).
- 29 Kim, K. *et al.* Optical diffraction tomography techniques for the study of cell pathophysiology. *Journal of Biomedical Photonics & Engineering* **2**, 020201 (2016).
- 30 Kim, K. *et al.* Three-dimensional label-free imaging and quantification of lipid droplets in live hepatocytes. *Scientific reports* **6**, 36815 (2016).
- 31 Ding, H., Wang, Z., Nguyen, F., Boppart, S. A. & Popescu, G. Fourier transform light scattering of inhomogeneous and dynamic structures. *Physical review letters* **101**, 238102 (2008).
- 32 Jung, J. H., Jang, J. & Park, Y. Spectro-refractometry of individual microscopic objects using swept-source quantitative phase imaging. *Anal Chem* **85**, 10519-10525, doi:10.1021/ac402521u (2013).
- 33 Kim, K. & Park, Y. Fourier transform light scattering angular spectroscopy using digital inline holography. *Optics letters* **37**, 4161-4163 (2012).
- 34 Yu, H., Park, H., Kim, Y., Kim, M. W. & Park, Y. Fourier-transform light scattering of individual colloidal clusters. *Optics letters* **37**, 2577-2579 (2012).
- 35 Song, K. *et al.* Smart gold nanoparticles enhance killing effect on cancer cells. *International journal of oncology* **42**, 597-608 (2013).
- 36 Lin, H. C. *et al.* Quantitative Measurement of Nano-/Microparticle Endocytosis by Cell Mass Spectrometry. *Angewandte Chemie International Edition* **49**, 3460-3464 (2010).
- 37 Betzer, O. *et al.* In-vitro Optimization of Nanoparticle-Cell Labeling Protocols for In-vivo Cell Tracking Applications. *Scientific reports* **5** (2015).
- 38 Jung, J. *et al.* Biomedical applications of holographic microspectroscopy [Invited]. *Applied optics* **53**, G111-G122 (2014).
- 39 Jung, J.-H., Jang, J. & Park, Y. Spectro-refractometry of individual microscopic objects using swept-source quantitative phase imaging. *Analytical chemistry* **85**, 10519-10525 (2013).
- 40 Sung, Y. *et al.* Optical diffraction tomography for high resolution live cell imaging. *Optics express* **17**, 266-277 (2009).
- 41 Kim, K., Yoon, J. & Park, Y. Simultaneous 3D visualization and position tracking of optically trapped particles using optical diffraction tomography. *Optica* **2**, 343-346 (2015).
- 42 Wolf, E. Three-dimensional structure determination of semi-transparent objects from holographic data. *Optics Communications* **1**, 153-156 (1969).
- 43 Patra, C. R., Bhattacharya, R., Mukhopadhyay, D. & Mukherjee, P. Fabrication of gold nanoparticles for targeted therapy in pancreatic cancer. *Advanced drug delivery reviews* **62**, 346-361 (2010).
- 44 Lim, J. *et al.* Comparative study of iterative reconstruction algorithms for missing cone problems in optical diffraction tomography. *Optics Express* **23**, 16933-16948, doi:10.1364/Oe.23.016933 (2015).
- 45 Kim, K. *et al.* High-resolution three-dimensional imaging of red blood cells parasitized by *Plasmodium falciparum* and in situ hemozoin crystals using optical diffraction tomography. *J. Biomed. Opt.* **19**, 011005-011012 (2014).



## Figures

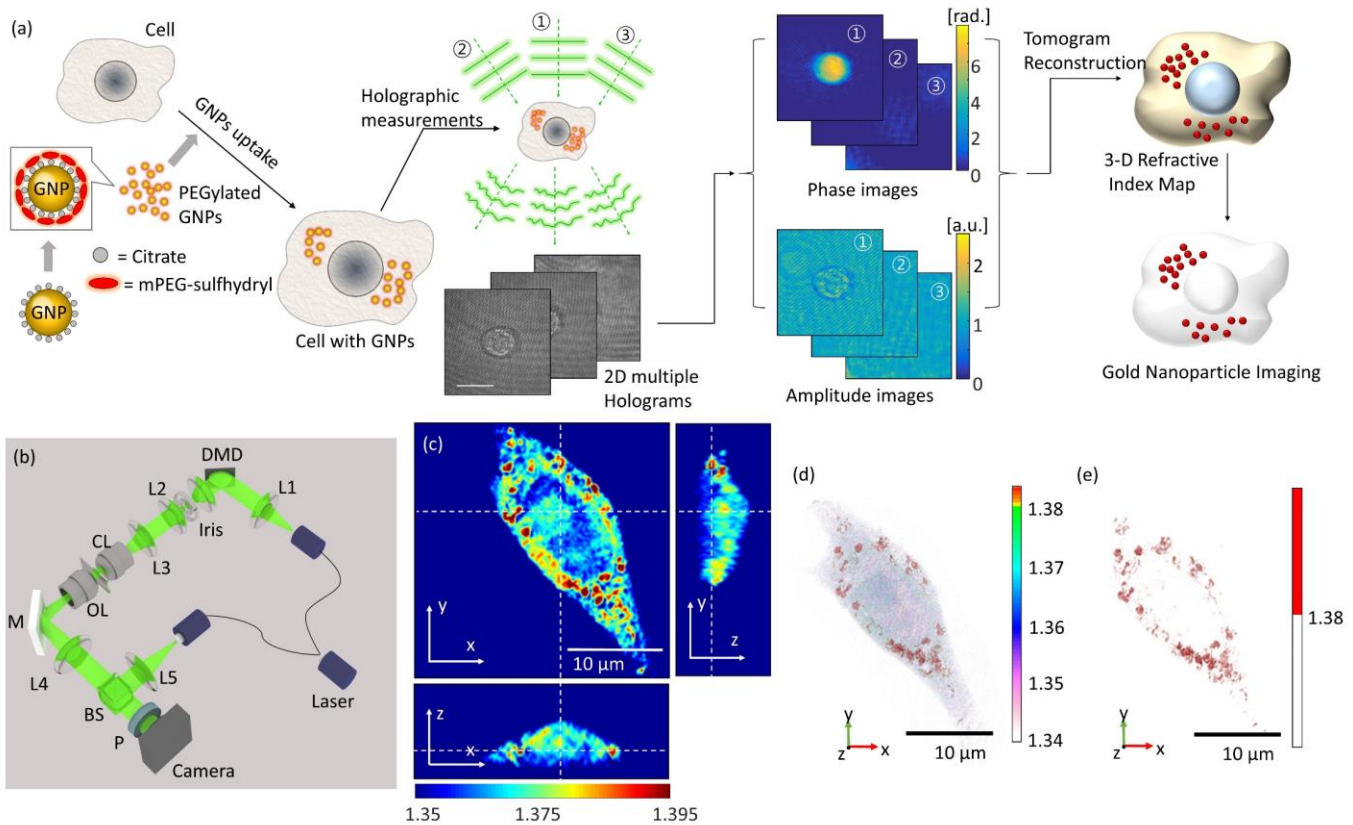


**Figure 1.** (a) Schematic procedure of imaging GNPs inside cells with ODT. (b) Optical setup. BS, beam splitter; DMD, digital micromirror device; OL, objective lens; CL, condenser lens; M, mirror; P, polarizer; L1-5, lenses. (c) Cross-sectional slices of the 3-D RI tomogram in the  $x$ - $y$ ,  $x$ - $z$ , and  $y$ - $z$  planes of a HeLa cell treated with GNPs. (d) The 3-D rendered image of the same cell. (e) The 3-D rendered image of the cell with the RI values greater than 1.38, which are considered as GNPs.

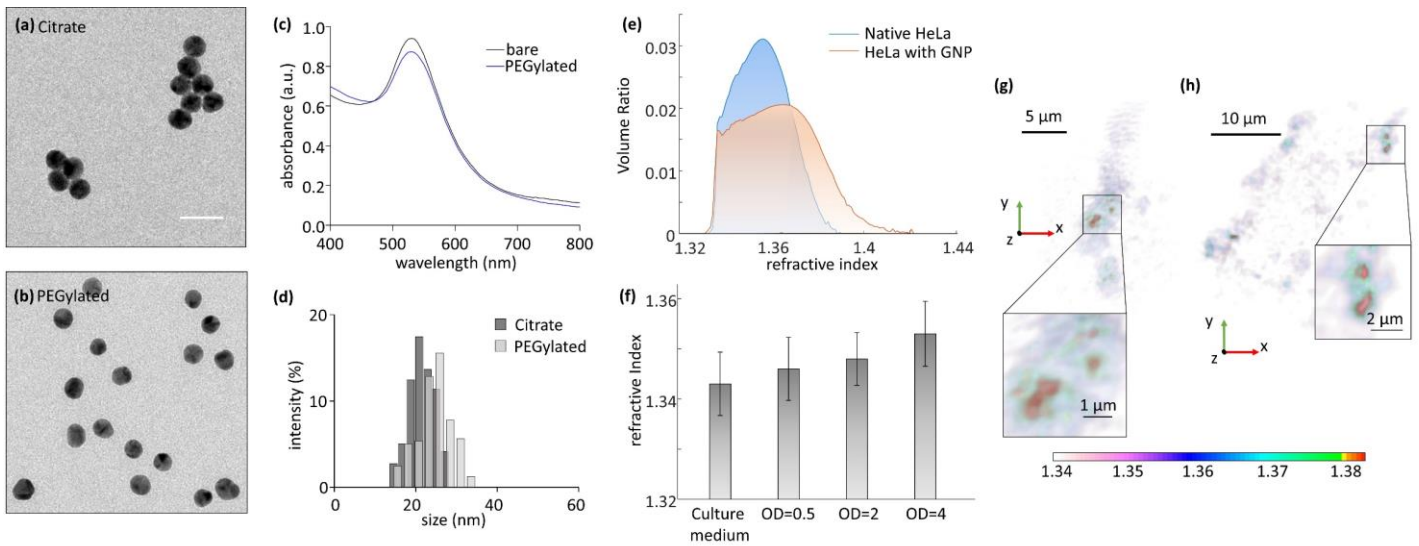


**Figure 2.** (a) Absorption spectra of citrated and PEGylated GNPs. (b) Hydrodynamic size distribution histogram of citrated and PEGylated GNPs. The size distribution histogram was obtained based on dynamic light scattering measurements. (c) Transmission electron microscopic (TEM) images of citrate and (d) PEGylated GNPs with average diameters of 20 nm. Scale bar is 50 nm. (e) Average RI histograms of GNPs treated ( $n = 15$ ) and native cells ( $n = 15$ ). (f) RI values of GNPs solutions with different concentrations of GNPs (OD values). Refractive index was measured with Fourier transform light scattering (FTLS). (g) 3-D rendered RI tomograms of aggregated GNPs.

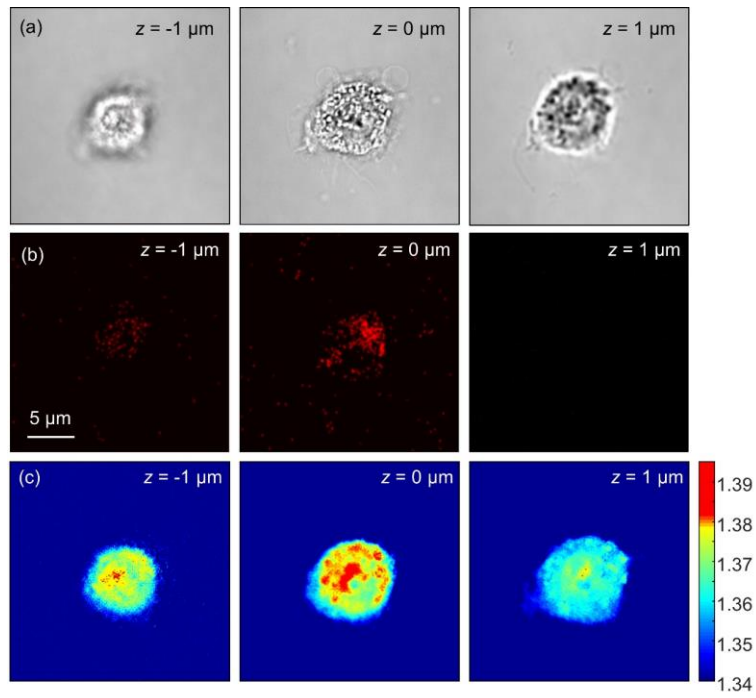


**Figure 3.** (a) Differential interference contrast (DIC) microscopic images of a HeLa cell treated with GNPs on different focal planes. (b) Confocal microscopic images of the same cell on same focal planes. (c)  $x$ - $y$  cross sections of the RI tomogram of the same cell on same planes.

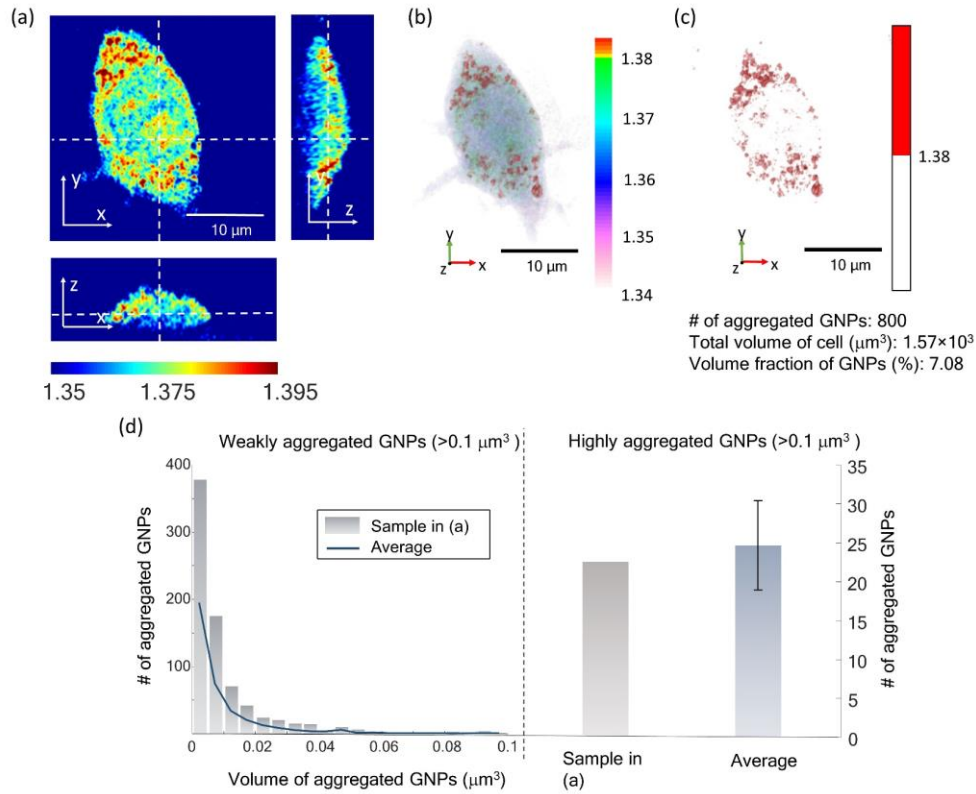


**Figure 4.** (a) Cross-sectional slices of the 3-D RI tomogram in the  $x$ - $y$ ,  $x$ - $z$ , and  $y$ - $z$  planes of a HeLa cell treated with GNPs. (b) The 3-D rendered image of the same cell. (c) The 3-D rendered image of the cell with the RI values greater than 1.38, which are considered as GNPs. (d) Volume distribution of aggregated GNPs inside HeLa cells.

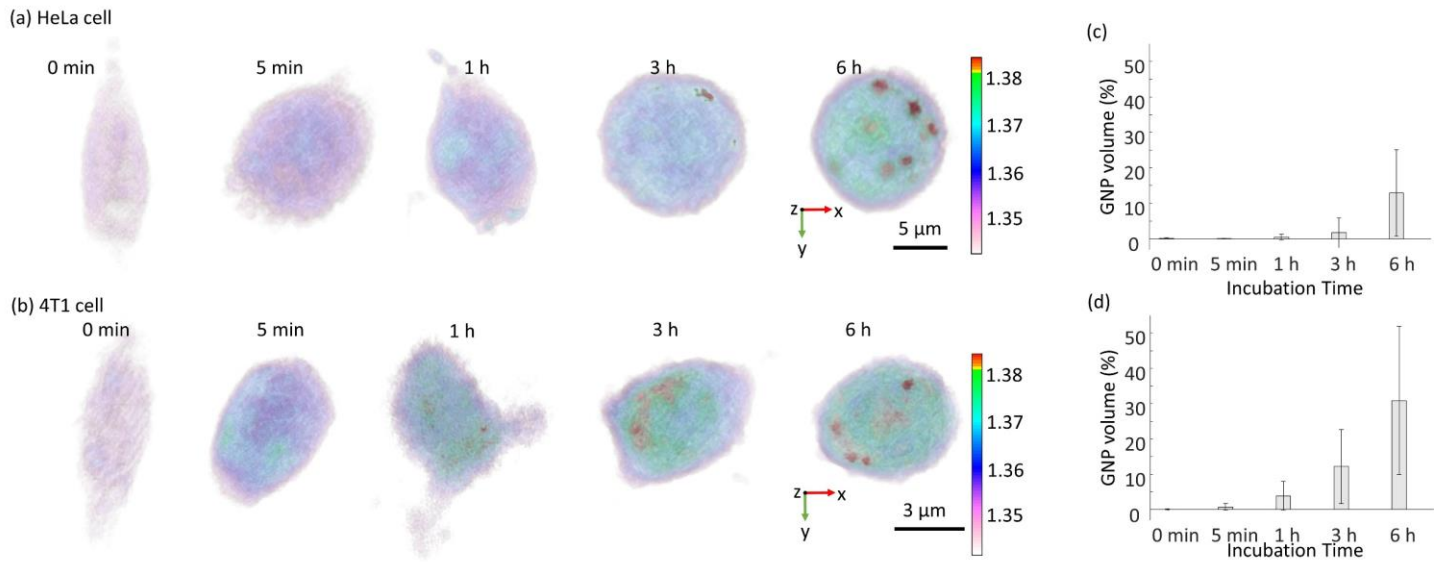


**Figure 5.** (a) 3-D rendered RI tomograms of HeLa cells with different GNPs treatment time. (b) The average volume ratio of GNPs in HeLa cells along the treatment time. (c) 3-D rendered RI tomograms of 4T1 cells with different GNPs treatment times. (d) The average volume ratio of GNPs in 4T1 cells along the treatment time.